

Time Dependent Radiation Hydrodynamics on a Moving Mesh

Philip Chang¹, Shane W. Davis² and Yan-Fei Jiang(姜燕飞)³

¹ *Department of Physics, University of Wisconsin-Milwaukee, 3135 North Maryland Avenue, Milwaukee, WI 53211, USA; chang65@uwm.edu*

² *Department of Astronomy, University of Virginia, Charlottesville, VA 22904, USA; swd8g@virginia.edu*

³ *Center for Computational Astrophysics, Flatiron Institute, 162 Fifth Avenue, New York, NY, 10010, USA; yjiang@flatironinstitute.org*

Accepted XXX. Received YYY; in original form ZZZ

ABSTRACT

We describe the structure and implementation of a radiation hydrodynamic solver for MANGA, the moving-mesh hydrodynamics module of the large-scale parallel code, Charm N-body GrAvity solver (ChaNGa). We solve the equations of time dependent radiative transfer using a reduced speed of light approximation following the algorithm of Jiang et al (2014). By writing the radiative transfer equations as a generalized conservation equation, we solve the transport part of these equations on an unstructured Voronoi mesh. We then solve the source part of the radiative transfer equations following Jiang et al (2014) using an implicit solver, and couple this to the hydrodynamic equations. The use of an implicit solver ensure reliable convergence and preserves the conservation properties of these equations even in situations where the source terms are stiff due to the small coupling timescales between radiation and matter. We present the results of a limited number of test cases (energy conservation, momentum conservation, dynamic diffusion, linear waves, crossing beams, and multiple shadows) to show convergence with analytic results and numerical stability. We also show that it produces qualitatively the correct results in the presence of multiple sources in the optically thin case.

Key words: methods: numerical — radiative transfer — hydrodynamics

1 INTRODUCTION

Smooth particle hydrodynamics (SPH) is based upon the Lagrangian view of the Euler equations where the sampling of a fluid is determined from a finite number of particles, and fluid quantities like density and pressure are determined by computing a smoothing kernel over a number of neighbors. The Lagrangian nature of SPH allows it to conserve linear and angular momentum, but comes at the expense of comparatively poor resolution of shocks due to its smoothing nature. On the other hand, grid based methods have superior shock capturing abilities due to the use of Godonov schemes, but suffer from grid effects, e.g., the presences of grid direction can affect the conservation of linear and angular momentum.

Springel (2010, hereafter S10) developed an arbitrary Lagrangian-Eulerian or moving-mesh (MM) scheme in an effort to capture the best characteristics of both approaches. S10's scheme relies on a Voronoi tessellation to generate well-defined and unique meshes for an arbitrary distribution of points that deform continuously under the movement of the mesh generating points. Implemented into the

code, AREPO, it has been used to study a number of different astrophysical problems including cosmological galaxy formation (see for instance Vogelsberger et al. 2014), disks, and stellar mergers (Zhu et al. 2015; Ohlmann et al. 2016).

Aside from AREPO, a number of MM codes have been developed based on S10's scheme. These include TESS (Duffell & MacFadyen 2011), FVMHD3D (Gaburov et al. 2012), ShadowFax (Vandenbroucke & De Rijcke 2016), RICH (Yalinewich et al. 2015), DISCO (Duffell 2016), and MANGA (Chang et al. 2017). These MM schemes have also been extended to include magnetic fields (Pakmor et al. 2011; Mocz et al. 2014, 2016; Chang 2018, in preparation), better convergence (Pakmor et al. 2016a; Mocz et al. 2015), and new physics, such as cosmic rays (Pakmor et al. 2016b; Pfrommer et al. 2017). In addition, the general scheme of determining the geometry from an arbitrary collection of points has also led to derivative methods such as GIZMO (Hopkins 2015).

SPH and MM schemes are similar in their need to compute the nearest neighbors of a point. As a result of this similarity, the most prolific MM code, AREPO, is built on top of the SPH code, Gadget (Springel 2005). While Gadget is perhaps the most widely used SPH code in astrophysics, a similar SPH code, ChaNGa, has been under heavy develop-

ment over the last decade (Jetley et al. 2008, 2010; Menon et al. 2015). Betraying its galaxy formation origins, ChaNGa includes standard physics modules that have been ported from its predecessor, Gasoline, including metal line cooling, star formation, turbulent diffusion of metals and thermal energy, and supernovae feedback (Stinson et al. 2006; Shen et al. 2010). The most up-to-date description of the SPH algorithms in Gasoline and ChaNGa is given in Wadsley et al. (2017).

ChaNGa is also unique among astrophysical codes in that it uses the Charm++ language and run-time system (Kale & Krishnan 1996) for parallelization rather than a custom message-passing interface design. While other Charm++ based codes exist, e.g., ENZO and FVMHD3D (Gaburov et al. 2012), ChaNGa is by far the most mature. The use of Charm++ allows ChaNGa to demonstrate strong scaling on a single timestepping problem with 12 billion particles to 512K cores (with 93% efficiency) and on a multi-timestepping problem with 52 million particles to 128K cores on Blue Waters (Menon et al. 2015). In the era of exascale computing, such scalability is increasingly important.

Upon the ChaNGa codebase, we have recently developed MANGA, a MM hydrodynamic solver for ChaNGa (Chang et al. 2017). MANGA is largely based on the S10 scheme, but includes a different approach to generating the Voronoi mesh, the use of conserved variables rather than primitives to compute the face states, and various other improvements that have been proposed since the publication of S10. More recently, we have begun incorporating additional physics into MANGA that is geared toward the study of dynamical stellar problems, including various equations of state (EOSs) such as the HELMHOLTZ EOS (Timmes & Swesty 2000), the EOS from the stellar evolution code MESA (Paxton et al. 2011, 2013, 2015), and a nuclear equation of state (O’Connor & Ott 2010; Schneider et al. 2017). In addition, we have also recently developed a multistep scheme (Prust & Chang 2019).

Radiation also plays a role in dynamical stellar problems like tidal disruption of stars, stellar mergers, or common envelope evolution. To account for the physics of radiation, we implement a radiation hydrodynamics solver in MANGA. Radiation hydrodynamics solvers involve the solution to the radiative transfer (RT) equations and a coupling between the radiation and fluid via the momentum and energy equations.

The general RT equations involves seven variables (3+1 for space and time, one for frequency, and two for direction). As result, the full solution of radiation transfer has traditionally been viewed as computationally intractable. Hence, most schemes involve a moment formalism to solve the RT equations, which greatly reduced the number of equations that need to be solved. A number of different closures for the moment equations are possible, including the flux-limited diffusion (FLD) (Levermore & Pomraning 1981; Turner & Stone 2001; Krumholz et al. 2007; van der Holst et al. 2011) and more recently the M1 method (González et al. 2007; Commerçon et al. 2011; Skinner & Ostriker 2013; Rosdahl & Teyssier 2015). The M1 method has also been recently implemented in the MM code, AREPO (Kannan et al. 2019).

The assumption underlying these closures cannot account for arbitrary complex radiation fields and can produce qualitatively incorrect results. As these problems are rooted in the basic scheme and not mitigated by resolution,

alternative schemes have been proposed. One such scheme is the variable Eddington tensor (VET) method (Davis et al. 2012; Jiang et al. 2012). Here, short characteristics are used to compute the specific intensity at every time step, from which direct quadrature is used to compute the components of the Eddington tensor that is used to close the radiation moment equations (Hayes & Norman 2003; Davis et al. 2012; Jiang et al. 2012).

Short characteristics schemes rely on solving the time-independent RT equations, which requires a global iterative solve. While such a scheme for a regular mesh has been outlined in Davis et al. (2012), it is far from clear that an equivalent scheme is possible in an unstructured mesh. The need for a global solve also makes short characteristics schemes difficult to implement.

Recently, Jiang et al. (2014, hereafter JSD14) described an alternative scheme where they solve the time-dependent RT equation. The attractiveness of this scheme is that its speed is independent of the number of sources, gives the correct answer in both the optically thin and thick regimes, and is (fairly) straightforward to implement. Moreover, it can be written as a conservation equation, which makes it easy to adapt to finite volume methods on unstructured meshes and to MMs in particular. As we mentioned above, such schemes have traditionally been viewed as computationally intractable, but advances in computation have made this approach increasingly viable in frequency averaged (gray or multigroup) limits.

In this work, we extend the algorithm of JSD14 to MM and implement it in MANGA. The paper is organized as follows. We discuss radiation hydrodynamics on a MM in § 2, by summarizing the algorithm of Chang et al. (2017). We then discuss radiative transfer in § 2.1, including transport (§ 2.2), the implicit solution for sources (§ 2.3), and implementation of boundary conditions (§ 2.4) and radiation source (§ 2.5). We then demonstrate the performance of the method in § 3 with a limited number of test problems, including radiation and gas thermalization, radiation and gas momentum transfer, crossing beams, and multiple shadows. We summarize our conclusions and discuss future improvements in § 4.

2 RADIATION HYDRODYNAMICS ON A MOVING VORONOI TESSELLATION

MANGA solves the Euler equations and energy evolution equation¹, which written in conservative form is:

$$\frac{\partial \rho}{\partial t} + \nabla \cdot \rho \mathbf{v} = 0 \quad (1)$$

$$\frac{\partial \rho \mathbf{v}}{\partial t} + \nabla \cdot \rho \mathbf{v} \mathbf{v} + \nabla P = -\rho \nabla \Phi \quad (2)$$

$$\frac{\partial \rho e}{\partial t} + \nabla \cdot (\rho e + P) \mathbf{v} = -\rho \mathbf{v} \cdot \nabla \Phi \quad (3)$$

where ρ is the density, \mathbf{v} is the velocity, Φ is the gravitational potential, $e = \epsilon + v^2/2$ is the specific energy, ϵ is the internal

¹ Following S10, we also include an evolution equation for entropy and switch between the two solutions either based on detections of shocks or explicit user input. In this work, we exclusively use energy evolution.

energy, and $P(\rho, \epsilon)$ is the pressure. Equations (1) - (3) can be written in a compact form by introducing a state vector $\mathbf{U} = (\rho, \rho\mathbf{v}, \rho\epsilon)$:

$$\frac{\partial \mathbf{U}}{\partial t} + \int \nabla \cdot \mathcal{F} dV = \mathcal{S} \quad (4)$$

where $\mathcal{F} = (\rho\mathbf{v}, \rho\mathbf{v}\mathbf{v}, (\rho\epsilon + P)\mathbf{v})$ is the flux function, and $\mathcal{S} = (0, -\rho\nabla\Phi, -\rho\mathbf{v} \cdot \nabla\Phi)$ is the source function.

S10 showed that equation (4) can be solved using a finite volume strategy on a moving unstructured mesh. Moreover, any equation that can be written in this generic form can be solved on moving unstructured meshes. For instance, the MHD equations can also be cast in this form (Pakmor et al. 2011; Duffell & MacFadyen 2011; Gaburov et al. 2012; Mocz et al. 2014, 2016). We refer the interested reader to S10 and Chang et al. (2017) for a more detailed discussion of the scheme. Here, we will only briefly describe the scheme to document the algorithm we have implemented and to highlight the differences between the scheme and that of S10 and highlight more recent development since the publication of Chang et al. (2017).

For each cell, the integral over the volume of the i th cell defines the charge of the i th cell, U_i , to be

$$U_i = \int_i \mathbf{U} dV = \mathbf{U}_i V_i, \quad (5)$$

where V_i is the volume of the cell. As in S10, we then use Gauss' theorem to convert the volume integral over the divergence of the flux in equation (4) to a surface integral:

$$\int_i \nabla \cdot \mathcal{F} dV = \int_i \mathcal{F} \cdot \hat{\mathbf{n}} dA \quad (6)$$

We now take advantage of the fact that the volumes are Voronoi cells with a finite number of neighbors to define an integrated flux

$$\sum_{j \in \text{neighbors}} \mathbf{F}_{ij} A_{ij} = \int_i \mathcal{F} \cdot \hat{\mathbf{n}} dA, \quad (7)$$

where \mathbf{F}_{ij} and A_{ij} are the average flux and area of the common face between cells i and j . The discrete time evolution of the charges in the system is given by:

$$U_i^{n+1} = U_i^n + \Delta t \sum_j \hat{\mathbf{F}}_{ij} A_{ij} + \Delta t \mathcal{S}_i, \quad (8)$$

where $\hat{\mathbf{F}}_{ij}$ is an estimate of the half-timestep flux between the initial, U_i^n , and final states U_i^{n+1} , and $\mathcal{S}_i^{(n+1/2)} = \int_i \mathcal{S} dV$ is the time-averaged integrated source function.

The steps that we perform to solve equation (8) are as follows:

(i) Estimate the Courant-limited timestep for each cell. We refer the reader to Chang et al. (2017) for details. The timestep can either be an individual timestep in a multi-step algorithm (Prust & Chang 2019) or a global time step (Chang et al. 2017).

(ii) Estimate the half time step state of the cell in two ways.

(a) Use the methodology of S10 as described in (Chang et al. 2017). Here, we estimate the gradients of the conserved quantities and use these to estimate the half-time-step conserved quantities via equation (4).

(b) Alternatively, solve the RHS of equation (8), but with the replacement of $\Delta t \rightarrow \Delta t/2$. Solve for the fluxes following the methodology described below, but use piecewise continuous reconstruction, instead of the piecewise linear reconstruction done for the full step. This method follows the time integration method in Athena++ as describe in White et al. (2016) and is called the van Leer method. We used this method for this work.

(iii) Drift the mesh generating points by a half-time step and recompute the half-time step tessellation. This is needed to provide second order convergence in time and follows the same idea as Duffell & MacFadyen (2011) and Pakmor et al. (2016a).

(iv) Use the half-time-step state to compute the half-time-step fluxes (described below) and apply the full step. Include changes due to the source terms (using the half-step values in the van Leer method).

(v) Update the state of the cell to the full step.

The inclusion of the van Leer half-step prediction is a development in this paper. The advantage of this method is that source terms are automatically included at second order and it greatly simplifies the code as the equations are only written once as opposed to the previous method where both the integral and differential forms of the equations must be written. This is especially important in radiation as the source term must be integrated implicitly (as discussed below). The van Leer method can be easily adapted to multistep schemes. The only change is that the ‘‘half-step’’ estimate must be taken from the cell’s initial state. However, we will only use global time-step in the remainder of this paper.

To estimate the flux across each face, $\hat{\mathbf{F}}_{ij}$, we use an approximate Riemann solver. As Riemann solvers for irregular cells in multidimensions do not exist, we follow the prescription of S10. We compute the 1-D fluxes across each face in the rest frame of that face and then collectively apply them per timestep. The steps involved are:

(i) Estimate the velocity $\tilde{\mathbf{w}}_{ij}$ of the face – following S10, the face velocities are:

$$\tilde{\mathbf{w}}_{ij} = \frac{(\mathbf{w}_i - \mathbf{w}_j) \cdot (\tilde{\mathbf{r}}_{ij} - 0.5(\mathbf{r}_j + \mathbf{r}_i))}{|\mathbf{r}_j - \mathbf{r}_i|} \frac{\mathbf{r}_j - \mathbf{r}_i}{|\mathbf{r}_j - \mathbf{r}_i|} + \bar{\mathbf{w}}_{ij}, \quad (9)$$

where $\bar{\mathbf{w}}_{ij} = 0.5(\mathbf{w}_i + \mathbf{w}_j)$ is the average velocity of the two mesh generating points and $\tilde{\mathbf{r}}_{ij}$ is the face center between cells i and j .

(ii) Estimate the state vector (in the rest frame of the moving face) at the face center ($\tilde{\mathbf{r}}_{ij}$) between the neighboring i and j cells via linear reconstruction.

(iii) Boost the state vector from the ‘‘lab’’ frame to the rest frame of the face center and rotate the state vector such that the x-axis points along the outward normal of the face, i.e., in the direction from i to j .

(iv) Estimate the flux using an HLL or HLLC (or HLLD for MHD; Miyoshi & Kusano 2005) Riemann solver implemented following Toro (2009). Here we found that both Riemann solvers give acceptable performance, though the HLL solver is more diffusive for problems that involve large gradients integrated over long timescale, i.e., hydrostatic balance. By default, we choose HLLC (or HLLD for MHD).

(v) Boost the solved flux back into the ‘‘lab’’ frame.

2.1 Radiative Transfer

We are interested in flows that are slow compared to the speed of light. Thus, we will adopt the reduced speed of light approximation in this paper. There are two key steps that are required to include radiation in MANGA. First, the radiation field, must be solved. Second the source function for the radiation must be computed using the solution of the radiation field. For the first step, the equation of radiative transfer in the reduced speed of light approximation is:

$$\frac{\partial I}{\partial t} + \bar{c} \hat{\mathbf{n}}_r \cdot \nabla I = S_r, \quad (10)$$

where S_r is the source function in the lab frame and \bar{c} is the reduced speed of light. For non-relativistic flows, it is usually sufficient to expand out the terms to $O(\beta)$ (Mihalas & Klein 1982). An interested reader is referred to JSD14 for an explicit expression of this source term. Here we refrain from writing the explicit expression, but note that lab frame radiation source term can be rewritten entirely in terms of variables evaluated in the fluid comoving (COM) frame using Lorentz transformations (see also Jiang et al. 2017). Here quantities represent frequency integrated (grey) expressions with $I \equiv \int I_\nu d\nu$, but our treatment easily generalizes to multiple independent frequency groups $I_j \equiv \int_{\nu_j}^{\nu_{j+1}} I_\nu d\nu$.

The zeroth, first, and second moments of the intensity, I , are

$$J \equiv \frac{1}{4\pi} \int I d\Omega, \quad (11)$$

$$\mathbf{H} \equiv \frac{1}{4\pi} \int \hat{\mathbf{n}}_r I d\Omega, \quad (12)$$

$$\mathbf{K} \equiv \frac{1}{4\pi} \int \hat{\mathbf{n}}_r \hat{\mathbf{n}}_r I d\Omega. \quad (13)$$

Since the moments are frequency integrated, they relate to the radiation energy density, radiation flux, and radiation pressure tensor via

$$E_r = \frac{4\pi}{c} J, \quad (14)$$

$$\mathbf{F}_r = 4\pi \mathbf{H}, \quad (15)$$

$$\mathbf{P}_r = \frac{4\pi}{c} \mathbf{K}. \quad (16)$$

Note that c in these equations is *by definition* the actual speed of light even when a reduced speed of light \bar{c} is used in equation (10). Taking zeroth and first moments of equation (10), we arrive at the equations for radiation energy and momentum conservation

$$\frac{c}{\bar{c}} \frac{\partial E_r}{\partial t} + \nabla \cdot \mathbf{F}_r = \int S_r d\Omega, \quad (17)$$

$$\frac{c}{\bar{c}} \frac{\partial (c^{-2} \mathbf{F}_r)}{\partial t} + \nabla \cdot \mathbf{P}_r = \frac{1}{c} \int S_r \hat{\mathbf{n}}_r d\Omega, \quad (18)$$

which reduce to standard expressions when $\bar{c} = c$. The quantities inside the time derivatives correspond to the energy and momentum densities of the radiation field. The source terms on the right hand side of this equation represent the net gain/loss of energy and momentum from the gas and the negative of these terms must be added as source terms on the right hand side of the gas energy and momentum equations. We note that the reduced speed of light approximation does not conserve total energy and momentum between the gas and radiation, which we elaborate on below.

2.2 Transport Step

Equation (10) can be written in terms of a conservation equation, e.g., equation (4), which makes it amendable to be solved on a moving Voronoi mesh. In particular, the state vector for radiation $\mathbf{U}_{\text{rad}} = (I_1, \dots, I_N)$, where N is the total number of intensities in angular and frequency space. The corresponding flux is $\mathcal{F}_{\text{rad}} = \bar{c}(\hat{\mathbf{n}}_{r,1} I_1, \dots, \hat{\mathbf{n}}_{r,N} I_N)$. Written this way, radiative transfer can be solved in two parts: transport and sources.

The transport step is solved similarly to the hydrodynamic transport step. In particular, the steps are:

(i) Estimate the velocity $\tilde{\mathbf{w}}_{ij}$ of the face – same as the hydrodynamic steps and given by equation (9).

(ii) Estimate the half-timestep state vector (in the rest frame of the moving face) at the face center ($\tilde{\mathbf{r}}_{ij}$) between the neighboring i and j cells via linear reconstruction – same as the hydro step and uses the same limiter as described in Chang et al. (2017).

(iii) Transform the radiative flux to the moving face frame: $\mathcal{F} = (\bar{c} \hat{\mathbf{n}}_r - \tilde{\mathbf{w}}_{ij}) I$.

(iv) Calculate flux using a simple upwind solver.

We note that the transport part of the radiative transfer equation is even easier than the hydrodynamic solution. In particular, no rotations to the moving face is necessary and the fluxes are simple upwind fluxes that do not require an approximate Riemann solver.

2.3 Implicit Solver and Hydrodynamic Source Terms

Having dealt with the transport part of the radiative transfer equation, we now turn to the source terms. As discussed above, the source terms are usually expanded out to $O(v/c)$ for non-relativistic flows. However, if we perform Lorentz boosts to and from the fluid COM frame, the system can be solved in a covariant fashion. In addition to being accurate to all orders in v/c , this procedure obviates the need to evaluate higher order angular moments. Here our COM frame is the center of momentum frame for the fluid element. This approach is the same as described in Jiang et al. (2017). The portion of the transfer equation corresponding to the source term update in the lab frame is given by

$$\frac{\partial I}{\partial t} = S_r = \bar{c} \rho \left(\kappa_P \frac{d\Gamma^4}{4\pi} + \kappa_S J - (\kappa_J + \kappa_S) I \right), \quad (19)$$

where κ_P and κ_J are the Planckian and mean absorption opacity respectively. We assume isotropic scattering (in the comoving frame) with scattering opacity κ_S . Note that all quantities in the above expression (including the opacities) are defined in the lab frame. This means that the opacities are not isotropic in this frame and motivates rewriting the source term in terms of COM frame variables.

The Lorentz transformation of the frequency between the lab and COM frame is given by

$$\frac{\nu}{\bar{\nu}} \equiv \Gamma = \gamma \left(1 - \frac{\mathbf{v} \cdot \hat{\mathbf{n}}_r}{c} \right), \quad (20)$$

where γ is the Lorentz factor (Rybicki & Lightman 1986). The specific intensities I_ν and extinction coefficients $\alpha_\nu =$

κ, ρ then transform according to

$$\tilde{I}_\nu = \Gamma^3 I_\nu, \quad (21)$$

$$\tilde{\alpha}_\nu = \Gamma^{-1} \alpha_\nu. \quad (22)$$

Since our intensities represent frequency integrated quantities ($I = \int I_\nu d\nu$), they transform with an additional power of Γ

$$\tilde{I} = \Gamma^4 I. \quad (23)$$

We also need to transform the weights associated with each angle to the comoving frame since integrals over angle are replaced with sums over these weights. Weights \mathcal{W} correspond to solid angle elements $d\Omega$, which transform as ν^{-2} . Hence,

$$\tilde{\mathcal{W}}_i = \mathcal{N} \frac{\mathcal{W}}{\Gamma^2}, \quad (24)$$

where \mathcal{N} is a normalization factor that ensures that $\sum_i \tilde{\mathcal{W}}_i = 1$ and $\tilde{J} = \sum_i \tilde{\mathcal{W}}_i \tilde{I}_i$, while accounting for the correct relative weighting of different angles in the comoving frame

We can now rewrite equation (19) using COM frame variables as

$$\frac{\partial \tilde{I}}{\partial t} = \tilde{S}_r = \Gamma(\hat{\mathbf{n}}_r) \tilde{c} \rho \left(\kappa_P \frac{a T^4}{4\pi} + \kappa_s \tilde{J} - (\kappa_J + \kappa_s) \tilde{I} \right), \quad (25)$$

where our convention is to denote comoving frame quantities with a tilde, with the exception of opacities which from this point onward are always defined in the COM frame where they are isotropic. Note that this is *not* the comoving frame transfer equation. Since the COM frame is a non-inertial frame it would contain additional terms related to acceleration that are not included here. Since we have instead rewritten the lab frame equation with COM frame variables, we have instead picked up a factor of $\Gamma(\hat{\mathbf{n}}_r)$, where $\hat{\mathbf{n}}_r$ denotes directions in the lab frame.

Frequency and angle integration of equation (19) yields an expression for the radiation energy equation, which couples to the gas internal energy equation

$$\frac{\rho k_B}{\mu(\gamma - 1)m_p} \frac{\partial T}{\partial t} = -c\rho \left(\kappa_P a T^4 - 4\pi \kappa_J \tilde{J} \right). \quad (26)$$

The relevant timescale for this set of equations is the thermalization time (between gas and radiation) which can be exceedingly short. As noted in JSD14, to keep the solver stable over reasonable timesteps, the equations must be solved implicitly.

Generalizing to the case with multiple frequency groups, we can proceed to discretize equation (25) with an implicit form as

$$\frac{\tilde{I}_{i,j}^{n+1} - \tilde{I}_{i,j}^n}{\Delta t} = \tilde{c} \Gamma_i \rho \left(\kappa_{P,j} \frac{a(T^{n+1})^4}{4\pi} + \kappa_{s,j} \tilde{J}_j^{n+1} - (\kappa_{J,j} + \kappa_{s,j}) \tilde{I}_{i,j}^{n+1} \right), \quad (27)$$

where integers n , i , and j denote timestep, angle, and frequency, respectively. Here, we assume that the coupling between different frequency bins occurs only through the $(T^{(n+1)})^4$ term. Solving for $\tilde{I}_{i,j}^{n+1}$ yields

$$\tilde{I}_{i,j}^{n+1} = \frac{\tilde{I}_{i,j}^n + \Delta t \tilde{c} \Gamma_i \rho \left(\kappa_{P,j} \frac{a(T^{n+1})^4}{4\pi} + \kappa_{s,j} \tilde{J}_j^{n+1} \right)}{1 + \Delta t \tilde{c} \Gamma_i \rho (\kappa_{J,j} + \kappa_{s,j})}. \quad (28)$$

To proceed, we sum $\tilde{I}_{i,j}^{n+1}$ over angle, using solid angle weighting factors $\tilde{\mathcal{W}}_i$ to obtain $\tilde{J}_j^{n+1} = \sum_i \tilde{\mathcal{W}}_i \tilde{I}_{i,j}^{n+1}$ and solve for

$$\tilde{J}_j^{n+1}$$

$$\tilde{J}_j^{n+1} = \frac{\Sigma_{\tilde{J}} + \Sigma_{\Gamma} \Delta t \tilde{c} \kappa_{P,j} \frac{a(T^{n+1})^4}{4\pi}}{1 - \Delta t \tilde{c} \rho (\kappa_{J,j} + \kappa_{s,j}) \Sigma_{\Gamma}}, \quad (29)$$

where we have defined

$$\Sigma_{\tilde{J}} \equiv \sum_i \frac{\tilde{I}_{i,j}^n \tilde{\mathcal{W}}_i}{1 + \Delta t \tilde{c} (\kappa_{J,j} + \kappa_{s,j}) \Gamma_i}, \quad (30)$$

$$\Sigma_{\Gamma} \equiv \sum_i \frac{\Gamma_i \tilde{\mathcal{W}}_i}{1 + \Delta t \tilde{c} (\kappa_{J,j} + \kappa_{s,j}) \Gamma_i}. \quad (31)$$

We can discretize equation (26) as

$$\frac{\rho k_B}{\mu(\gamma - 1)m_p} \frac{T^{n+1} - T^n}{\Delta t} = \sum_j \mathcal{W}_j c \rho \left(4\pi \kappa_{J,j} \tilde{J}_j^{n+1} - \kappa_{P,j} a (T^{n+1})^4 \right), \quad (32)$$

where \mathcal{W}_j denotes possible weights for different frequency groups. We can now eliminate \tilde{J}_j^{n+1} using equation (29) and solve directly for T^{n+1} . For a temperature independent opacity, this yields a quartic equation for T^{n+1} , which we solve analytically. For a temperature dependent opacity, we use Newton-Raphson iteration to arrive at a solution. We have tested both methods for temperature independent opacities and found that they yield equivalent results.

Finally, we compute the radiation moments for frequency group j and timestep n via

$$E_{r,j}^n = \frac{4\pi}{c} \sum_i \mathcal{W}_i I_{i,j}^n, \quad (33)$$

$$\mathbf{F}_{r,j}^n = 4\pi \sum_i \mathcal{W}_i \hat{\mathbf{n}}_{r,i} I_{i,j}^n. \quad (34)$$

The implementation of the algorithm proceeds as follows:

(i) Compute lab frame values for the radiation energy density $E_{r,j}^n$ and flux $\mathbf{F}_{r,j}^n$ at beginning of the source term step using equations (33) and (34).

(ii) Transform $I_{i,j}^n$ to $\tilde{I}_{i,j}^n$ using equation (23), perform the sums over angle needed to evaluate equation (29), and solve equation (32) for T^{n+1} .

(iii) For each angle and frequency (if using multiple groups) evaluate $\tilde{I}_{i,j}^{n+1}$ with equation (28) and use equation (23) to transform $\tilde{I}_{i,j}^{n+1}$ to $I_{i,j}^{n+1}$.

(iv) Evaluate new lab frame values $E_{r,j}^{n+1}$ and $\mathbf{F}_{r,j}^{n+1}$ and compute the changes for the gas energy and momentum via

$$\Delta E = \frac{c}{\tilde{c}} \sum_j \mathcal{W}_j \left(E_{r,j}^n - E_{r,j}^{n+1} \right) \quad (35)$$

$$\Delta(\rho \mathbf{v}) = \frac{1}{c\tilde{c}} \sum_j \mathcal{W}_j \left(\mathbf{F}_{r,j}^n - \mathbf{F}_{r,j}^{n+1} \right). \quad (36)$$

In other words, any loss of energy or momentum by the radiation field due to the source term coupling must correspond to a gain by gas to ensure energy conservation. The factors of c/\tilde{c} and $1/(c\tilde{c})$ are dictated by the form of equations (17) and (18). Finally, we should note that our use of equations (35) and (36) conserves $E_g + cE_{\text{rad}}/\tilde{c}$. Modified schemes can also be used to conserve $E_g + E_{\text{rad}}$, but they not as applicable to very optically-thick media.

2.3.1 Reduced Speed of Light Approximation

The equations above implement the reduced speed of light approximation (RSLA). In the limit $\bar{c} \rightarrow c$, we recover the standard radiation transfer equations. Notice that this does not mean the speed of light is reduced in all contexts, as c and \bar{c} both appear in equations in sections (2.1)-(2.3). For example, c appears on the right hand side of equation (26) whereas \bar{c} appears on the right hand side of equation (25). The logic of the RSLA is that for some problems the time variability of the radiation field on timescales short compared to the flow time can be incorrect as long as the time variability on driven by the flow is accurate captured.

This has important implications for energy and momentum conservation. If we add the radiation source term to the right hand side equation (3), then equation (17) implies

$$\frac{\partial}{\partial t} \left(\frac{c}{\bar{c}} E_r + \rho e \right) + \nabla \cdot [\mathbf{F}_r + (\rho e + P) \mathbf{v}] = -\rho \mathbf{v} \cdot \nabla \Phi. \quad (37)$$

Similarly, combining equations (2) and (18) yields

$$\frac{\partial}{\partial t} \left(\frac{\mathbf{F}_r}{c\bar{c}} + \rho \mathbf{v} \right) + \nabla \cdot (P_r + \rho \mathbf{v} \mathbf{v}) + \nabla P = -\rho \nabla \Phi. \quad (38)$$

This explains why equations (35) and (36) differ by a factor of c/\bar{c} from standard relations. We only get the standard relations for conservation of energy and momentum in the limit that $\bar{c} \rightarrow c$. This is the price we pay for ensuring that the quasisteady-state behavior of the radiation on flow timescales is correct.

As discussed in Skinner & Ostriker (2013) one must be careful to maintain the appropriate hierarchy of timescales when applying the RSLA. We can define a characteristic flow timescale of $t_{\text{fl}} \simeq L/v$ where L and v are characteristic flow lengths and velocities. We can also define timescales corresponding to radiation streaming and diffusion as $t_{\text{str}} \simeq L/\bar{c}$ and $t_{\text{dif}} \simeq L/(\bar{c}\tau)$ where $\tau \geq 1$ is the characteristic optical depth corresponding to length L . The RSLA is unlikely to provide reliable results when $t_{\text{fl}} < t_{\text{str}}$ so we must generally choose $\bar{c} > v$, where v is the largest flow velocity or sound speed. In problems with large optical depths, the more constraining relation is that we must also maintain $t_{\text{fl}} > t_{\text{dif}}$, which requires choosing $\bar{c} > v\tau$. This generally limits the advantage of applying the RSLA to optically thick flows.

2.4 Boundary Conditions

The original implementation of MANGA (Chang et al. 2017) only included periodic boundary conditions. By comparison AREPO has both reflecting and periodic boundary conditions (S10) and the reflecting boundary conditions can be arbitrarily placed and variable with time. For the radiation problems, it is useful to have some sort of outflow or radiation boundary condition for the test problems below. Here, we describe our implementation of outflow or absorbing and radiation boundary conditions as a source implementation.

To implement a form of absorbing boundaries, we mark certain cells as having boundaries where we desire the hydrodynamic and radiative primitive variables to be

$$\rho \rightarrow \rho_0 \quad \text{and} \quad \mathbf{v} \rightarrow 0 \quad \text{and} \quad I \rightarrow I_0 \equiv \frac{aT^4}{4\pi}, \quad (39)$$

where I_0 is the defined boundary radiation specific intensity,

which is direction dependent, and T_{eff} is the effective temperature of the radiation source. To achieve this, we impose the following source terms for the boundary cells:

$$\frac{\partial \rho}{\partial t} = S_\rho = \frac{\rho_0 - \rho}{\tau}, \quad (40)$$

$$\frac{\partial \rho \mathbf{v}}{\partial t} = S_{\rho \mathbf{v}} = -\frac{\rho \mathbf{v}}{\tau}, \quad (41)$$

$$\frac{\partial I}{\partial t} = S_I = -\frac{I - I_0}{\tau}, \quad (42)$$

where τ is a relaxation timescale, and is selected to be longer than the timestep, but much smaller than the typical timescales of interest. We note that the density and velocity source terms produces a source term for the energy as well, which is easily computed.

The discretized version of equations (40) - (42) gives the timestepping algorithm used in the boundary computation:

$$\rho^{n+1} = \rho^n + \min(\Delta t/\tau, 1)(\rho_0 - \rho^n), \quad (43)$$

$$\rho^{n+1} \mathbf{v}^{n+1} = \rho^n \mathbf{v}^n (1 - \min(\Delta t/\tau, 1)) \quad (44)$$

$$I^{n+1} = I^n - (I^n - I_0) \min(\Delta t/\tau, 1), \quad (45)$$

where the $\min(\Delta t/\tau, 1)$ limits the correction down to zero per timestep.

2.5 Radiation Sources

In addition to the boundary conditions implemented above, we also include radiation source terms in MANGA. These radiation source terms are defined in the comoving frame and is defined by a variant of equation (25).

$$\frac{\partial \tilde{I}}{\partial t} = \Gamma(\hat{\mathbf{n}}'_r) \bar{c} \rho \left(\kappa_{\text{P}} \frac{aT^4}{4\pi} - \kappa_{\text{P}} \tilde{I} \right), \quad (46)$$

where $\hat{\mathbf{n}}'_r$ is the user defined directions of interest. Here the power of the sources are defined in terms of local density and hence require some nontrivial opacity for it to radiate effectively. The combination of radiation source and radiation boundary conditions (described in § 2.4) allow us to study a wide range of different situations.

3 TEST PROBLEMS

We now demonstrate the accuracy of the radiation hydrodynamics solver in MANGA with a limited number of test problems. The implementation of MANGA currently limits it to 3-D problems. While one and two dimensional problems are possible for MANGA in principle, no such extension is planned.

3.1 Thermal Equilibrium

The thermal equilibration timescale in many astrophysical contexts can be much shorter than the dynamical time. Our use of an implicit integrator in the radiation source terms ensures that the solution will be stable for large timesteps (compared to the local thermal time). As a demonstration of the accuracy and stability of our implicit solver, we setup a 1 pc simulation cube and fill it with 3×10^4 particles. The box consists of atomic hydrogen with a density of $\rho = 10^{-15} \text{ g cm}^{-3}$ and initial temperature of $T = 10 \text{ K}$. The box is also filled with radiation at a initial radiation temperature

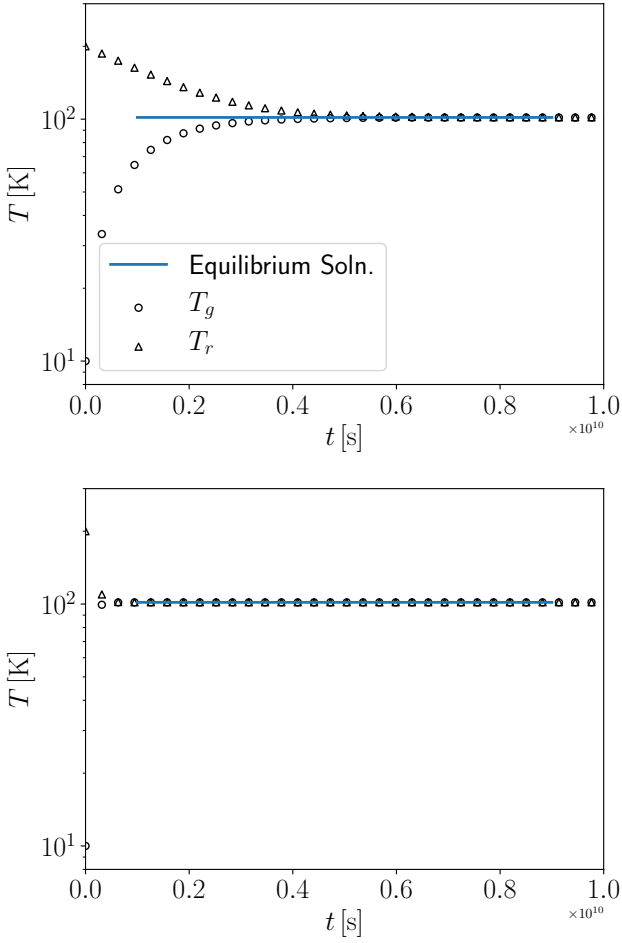


Figure 1. Gas (circles) and Radiation (triangles) Temperatures as a function of t for $\kappa = 1 \text{ cm}^2 \text{ g}^{-1}$ (top) and $\kappa = 100 \text{ cm}^2 \text{ g}^{-1}$ (bottom). The initial $T_r = 200 \text{ K}$, while the initial gas temperature is $T_g = 10 \text{ K}$. The solid blue line is the equilibration temperature of 101.7 K .

of $T = 200 \text{ K}$, which is substantially larger than the gas temperature. We set $\bar{c} = c$. We consider two cases. In the first case, we consider an equilibration time that is longer than the timestep. In the second case, we consider an equilibration time much shorter than the timestep. These two cases are achieved for exactly the same initial conditions by changing the opacity of the material, e.g., $\kappa = 1 \text{ cm}^2 \text{ g}^{-1}$ for the first case, $\kappa = 100 \text{ cm}^2 \text{ g}^{-1}$ for the second.

We plot in Figure 1 the evolution of the gas (circles) and radiation (triangles) temperatures as a function of time for $\kappa = 1 \text{ cm}^2 \text{ g}^{-1}$ (top plot) and $\kappa = 100 \text{ cm}^2 \text{ g}^{-1}$ (bottom plot). We also plot the expected equilibrium temperature as a solid blue line. For the $\kappa = 100 \text{ cm}^2 \text{ g}^{-1}$ case, the equilibration time is much smaller than the time step, but the implicit solver quickly produces the correct equilibration temperature nevertheless. This is perhaps unsurprising as the implicit solver determines the equilibration directly. However, it is reassuring that even in the presence of short thermalization times, MANGA produces the correct solution.

3.2 Momentum Conservation

Our scheme also displays excellent momentum conservation properties between radiation and gas. Similarly to the thermal equilibrium properties discussed above, our use of an implicit integrator in the radiation source terms ensure stability for large timesteps (compared to the local equilibration timescale). As an example, we now consider the same case as in § 3.1, but here we impose a radiation flux as oppose to perfectly isotropic radiation. We do this by imposing that only rays whose normal direction has a $\mu = \cos \theta \geq 0.8$ with the x-axis is populated. As a result the radiation contains a net momentum, which it will impart on the gas. Here, we again set $\bar{c} = c$. Again, we consider two cases, the case of long equilibration times, $\kappa = 1 \text{ cm}^2 \text{ g}^{-1}$, and that of short equilibration times, $\kappa = 100 \text{ cm}^2 \text{ g}^{-1}$. We plot in Figure 2 the evolution of the gas (empty circles) and radiation (triangles) effective velocities for radiation, \bar{v}_r , and gas, \bar{v}_g , as a function of time for $\kappa = 1 \text{ cm}^2 \text{ g}^{-1}$ and $\kappa = 100 \text{ cm}^2 \text{ g}^{-1}$, where we define

$$\bar{v}_r \equiv m_{\text{tot}}^{-1} \int \frac{\mathbf{F}_r}{c^2} dV \quad \text{and} \quad \bar{v}_g \equiv m_{\text{tot}}^{-1} \int \rho \mathbf{v} dV \quad (47)$$

We also plot the total momentum as solid black circles which is conserved with a maximum error fraction of 4×10^{-4} . For the $\kappa = 100 \text{ cm}^2 \text{ g}^{-1}$ case, the equilibration time is much smaller than the time step, but the implicit solver produces the proper momentum in the gas.

3.3 Dynamic Diffusion

A dynamic diffusion test is useful for testing the diffusion of radiation in an optically thick moving medium where both the advection and diffusion of radiation occurs simultaneously. Previously, JSD14 argued that the transport part of equation (10) should be split into a fluid advection term and a radiation transport term to reduce numerical diffusion for optically thick cells. Instead, we have adopted a van Leer second order time integration that allows us to pass this test without using the JSD14 split transport scheme.²

² We note that Athena++ also implements a van Leer scheme (White et al. 2016) and its utility in reducing numerical diffusion in optically thick media has already been demonstrated in that code.

We setup a uniform medium with background density $\rho = 10^{-2} \text{ g cm}^{-3}$ and box size in the x-direction $L_x = 3 \times 10^{10} \text{ cm}$ and resolve it with 128 cells. We set $x = 0$ to be the center of this domain. The box size in the y and z direction are equal, $L_y = L_z$ and set to be boxes that are $3dx$ across, where dx is the separation of grid points in the x-direction. These physical units are irrelevant to the problem once everything is scaled to the four parameters described below in § 3.6, e.g., $C = c/c_s$, the ratio between the speed of light and isothermal sound speed, $\mathcal{P} = P_{\text{rad}}/P_g$, the ratio between the radiation and gas pressures, $\tau = \kappa \rho L$, the optical depth in the x-direction. We setup the mesh-generation points with a regular lattice structure, but perturbed randomly by 10^{-6} of the grid spacing to ensure that there are no degeneracies in the Voronoi planes. The optical depth of the entire box is set to be $\tau = 400$. We set $\bar{c} = c$ and $c_s = 0.1c$ and the initial velocity of the flow to be $v_{x,0} = 0.1c$. We do not evolve the hydrodynamic quantities and allow the mesh to follow the flow.

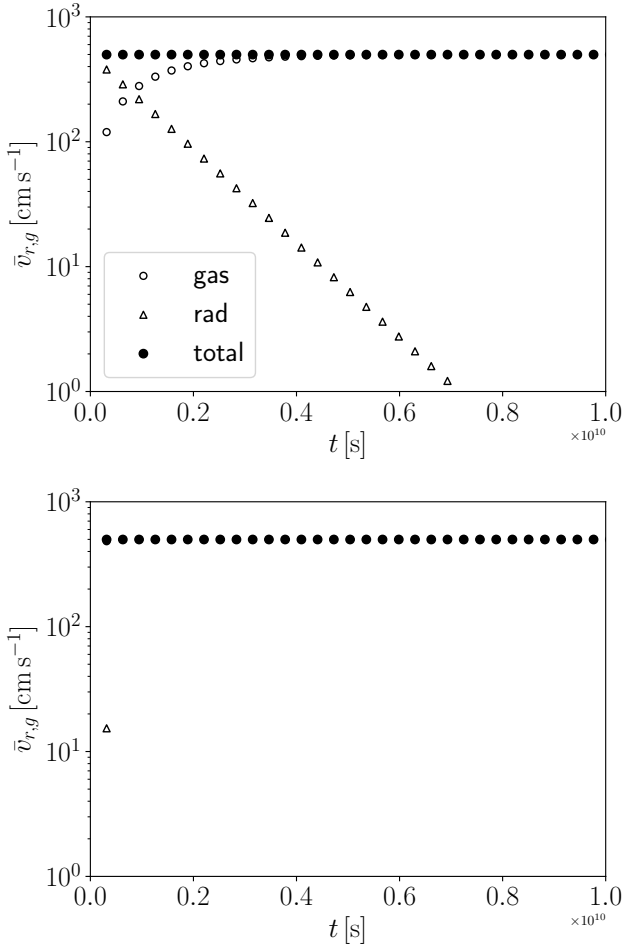


Figure 2. Gas (empty circles) and Radiation (triangles) effective velocities as a function of t for $\kappa = 1 \text{ cm}^2 \text{ g}^{-1}$ (top) and $\kappa = 100 \text{ cm}^2 \text{ g}^{-1}$ (bottom). The effective velocity for the total momentum is shown by filled circles. The momentum is conserved to better than 4×10^{-4} .

The initial profile of the radiation energy density and flux is set to be

$$E_r = E_{r,0} \exp\left(-\frac{x^2}{\Delta x^2}\right), \quad (48)$$

$$F_r = \frac{4v}{c} E_r, \quad (49)$$

As in JSD14, we limit the lower value of E_r to be fixed by $E_{r,0} \exp(-10)$ and like the linear wave test discussed below, we limit the number of angles to one per octant. We also ignore the diffusive flux term as in JSD14; we find it makes little difference. In the diffusion limit, the analytic solution is given by (JSD14)

$$E_r(x, t) = \frac{E_{r,0}}{\sqrt{4Lv_d t / \Delta x^2 + 1}} \exp\left(-\frac{x^2 / \Delta x^2}{4Lv_d t / \Delta x^2 + 1}\right). \quad (50)$$

In Figure 3, we plot E_r for the case of $t = 0.1, 0.5,$ and $1L/v_{x,0}$. We overplot the analytic solution given by equation (50). This Figure shows that our algorithm can calculate the diffusion and advection processes accurately without the splitting of the transport step as done in JSD14.

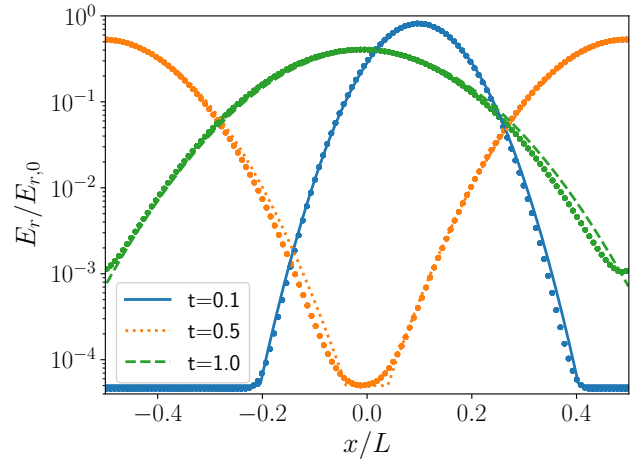


Figure 3. The radiation energy density, E_r , as a function of position for three different times of $t = 0.1, 0.5,$ and $1L/v_{x,0}$. The corresponding analytic solutions given by equation (50) are overplotted as solid, dotted, and dashed lines (respectively).

3.4 Crossing Beams

The propagation of two beams of radiation in vacuum is a straightforward test which can produce qualitatively wrong results depending on the radiative transfer method. For instance, M1 methods tend to merge two beams of radiation at point that they intersect due to there being a single preferred direction in this moment method (JSD14). Short characteristics methods (Davis et al. 2012; Jiang et al. 2012) and time dependent angular methods (JSD14), on the other hand, produce correct results.

In Figure 4, we show the results of the crossing beam test in our moving-mesh implementation. Here, we set $\bar{c} = 10 \text{ km s}^{-1}$ in a box that is 16 pc on a side and fill it with 3×10^5 particles by replication a glass distribution of 4,096 particles. We note that the actual values of the box and reduced speed of light is irrelevant here as the absorption and scattering opacities are minimal, e.g., $\tau < 1$ across the box. We use 80 angles in the simulation to cover the unit sphere. In this simulation, we do not perform an implicit solve for the gas temperature as describe in § 2.3, but rather leave it fixed. This allows us to focus on the propagation of radiation. We place sources as cylindrical sources along z at $(x, y) = (-10^{19}, -10^{19}) \text{ cm}$ and $(10^{19}, -10^{19}) \text{ cm}$ with directions of $\theta = \pi/4$ and $3\pi/4$ on the left and right cylinder respectively. We use a radiation temperature of $T_{\text{eff}} = 200 \text{ K}$. Here θ is defined along the x - y plane. The opening angle is set such that $\cos \delta\theta < 0.95$, which picks out just two angles per cylindrical source. Finally, we place an absorbing boundary condition at $y = 2 \times 10^{19} \text{ cm}$ and periodic boundary conditions in the x - z boundaries.

In the left plot, the fluid has zero velocity and we see that the results are qualitatively correct after several radiation crossing times. In the right plot, the fluid moves in the $+x$ direction at a velocity of $v = 3 \text{ km s}^{-1}$, which is 30% of the reduced speed of light \bar{c} . This motion of the fluid moves the cells in a MM code and some effect in light propagation is expected when the velocity of the fluid approaches the reduced speed of light. Here we find that after beams have

propagated there is little difference between the case where mesh generating points are static (left plot) and where they are moving (right plot) at 30% of the reduced speed of light. Though we do not show it, we did find that the radiation front is distorted in the direction of the mesh generating points' motion. Finally, distortions on the propagation of the beams show up when the mesh generating points approach 50% of the reduced speed of light or higher, which we also do not show. However, given the effect of slowly moving meshes (relative to \bar{c}) on equilibrium radiation fields is small, the reduced speed of light approximation is excellent when \bar{c} is set to be few times faster than the fastest fluid velocity and/or mesh generating points.

3.5 Shadow Test

Like the crossing beam test, the shadow test has been used to demonstrate the ability of various methods (FLD, M1, RT, VET) to capture the qualitatively correct behavior of photons propagating in multiple directions simultaneously. This test has been widely used to demonstrate the superiority of M1 methods to capture the shadow cast by one beam compared to FLD, which does not cast shadows (McKinney et al. 2014). However, M1 performs more poorly with more than one beam, e.g. multiple shadows. In particular, the closure used in M1 can only account for one direction of propagation. For more than one beam, the direction is then taken as the intensity weighted direction, which is qualitatively incorrect. On the other hand, time dependent methods (JSD14) or VET (Davis et al. 2012; Jiang et al. 2012) methods capture the correct qualitative dynamics.

We set up a multiple shadow simulation with a 16 pc side box and populate it with 3.1 M mesh-generating points. This simulation is larger than the others above because we want to capture the sharp transition between fluids of different densities. We set an ambient density of $\rho = 3 \times 10^{-22} \text{ g cm}^{-3}$ with a mean opacity of $\kappa_{\text{J}} = 100 \text{ cm}^2 \text{ g}^{-1}$, making it marginally optically thick, $\tau \approx 1$. The Planck opacity (corresponding to emission) is set much smaller $\kappa_{\text{p}} = 10^{-2} \text{ cm}^2 \text{ g}^{-1}$, so that there is negligible re-emission. As in the crossing beam test, we adopt periodic boundary conditions along the x and z axis. We use absorbing boundary conditions for the radiation and periodic boundary conditions for the gas. The exception is the lower y-boundary where we set the boundary to be a fixed radiation input field. The radiation is set at directions of $\theta = 0.98$ (56 degrees) and -0.98 , measured from the y-axis, and the radiation temperature is $T_{\text{eff}} = 200 \text{ K}$. At $(x, y) = (0, -3) \text{ pc}$, we place a dense elliptical tube that extends in the z-direction. We set the density of the tube to be 1000x larger than the ambient density so that it is optically thick. The elliptical tube has a major axis of 4.8 pc and a minor axis of 3 pc, with the major axis oriented along the x-axis. We adopt the same opening angle of $\cos \delta\theta < 0.98$, which picks out just one angle. Finally, we place absorbing boundary condition at the top and bottom (in y), but periodic elsewhere. We ignore the radiation coupling to the hydrodynamics though the hydrodynamics are evolved.

In Figure 5, we project E_r for the multiple shadow test. The multiple shadows cast by the tube is qualitative what is expected. the umbra and penumbra are visible and follow

our qualitative expectations. As argued in JSD14, these results are qualitatively superior to the M1 method, which casts only one shadow.

3.6 Linear Wave

The radiative linear wave is a full end-to-end test of the full radiation hydrodynamics algorithm and, thus, we carry out the linear wave test in a 3D domain based on the dispersion relation Jiang et al. (2012) (see also Jiang et al. 2014; Zhang et al. 2018). As discussed in Jiang et al. (2014), the relevant parameters for this test are $C = c/c_s$, the ratio between the speed of light and isothermal sound speed, $r = \bar{c}/c$, the ratio between the reduced speed of light and speed of light, $\mathcal{P} = P_{\text{rad}}/P_{\text{g}}$, the ratio between the radiation and gas pressures, $\tau_{\lambda} = \kappa\rho\lambda$, the optical depth over one wavelength, and $\gamma = 5/3$, the adiabatic gas index.

The setup in MANGA assume physical units, so we setup a uniform medium with background density $\rho = 10^{-2} \text{ g cm}^{-3}$ and box size in the x-direction $L_x = 3 \times 10^{10} \text{ cm}$. The box size in the y and z direction are equal, $L_y = L_z$ and set based on the resolution in the x-direction and scaled such that the total number of 3-d mesh generating points remains approximately constant. These physical units are irrelevant to the problem once everything is scaled to the four parameters described above. We setup the mesh-generation points with a regular lattice structure, but perturbed randomly by 10% of the grid spacing to ensure that there are no degeneracies in the Voronoi planes. We also fix the mesh-generating points in this test as the motion of the mesh generating points (in the regularization step, e.g. see Chang et al. 2017) produced noise that can exceed the perturbation of the linear wave.

Setting the wavelength of the linear wave to be the size of the box in the x-direction, we adopt $C = 1.45 \times 10^3$, $r = 10^{-2}$, and $\mathcal{P} = 1$. In other words, we use a reduced speed of light which is 1% of the speed of light and a sound speed that is ≈ 0.1 of the reduced speed of light. We also set the radiation pressure equal to the gas pressure. We have run tests with different r and \mathcal{P} and the results are consistent with the analytic results (using those parameters) that we describe below. We use the analytical solutions of Davis et al. (2012) for $\tau_{\lambda} = 10^{-2} - 10^2$ to initialize a linear wave with a dimensionless amplitude of 10^{-3} .

In Figure 6, we compare the measured phase velocity, v_{ph} in units of the isothermal sound speed, c_s , and the measured damping rate, γ , from our MANGA simulation with an effective grid resolution of 160 in the x-direction with the analytic curves from Zhang et al. (2018). We measure the phase velocity and damping rate by evolving our linear wave for one isothermal sound speed crossing time and fitting the linear wave solution for the phase and amplitude. It is clear from this figure that the analytic results are captured with a high fidelity.

In Figure 7, we plot the error, ϵ (with arbitrary normalization) as a function of the number of grid points in the x-direction, e.g., the effective resolution. Here we define the error, ϵ , as the L1 norm between the analytic and numerical solutions after one isothermal crossing time. A fit to the error shows that the convergence of the radiative linear wave (in all optical thickness regimes) is approximately a power law with an index of -1 . We confirm the second order nature of the hydrodynamics solver by showing the L1 norm

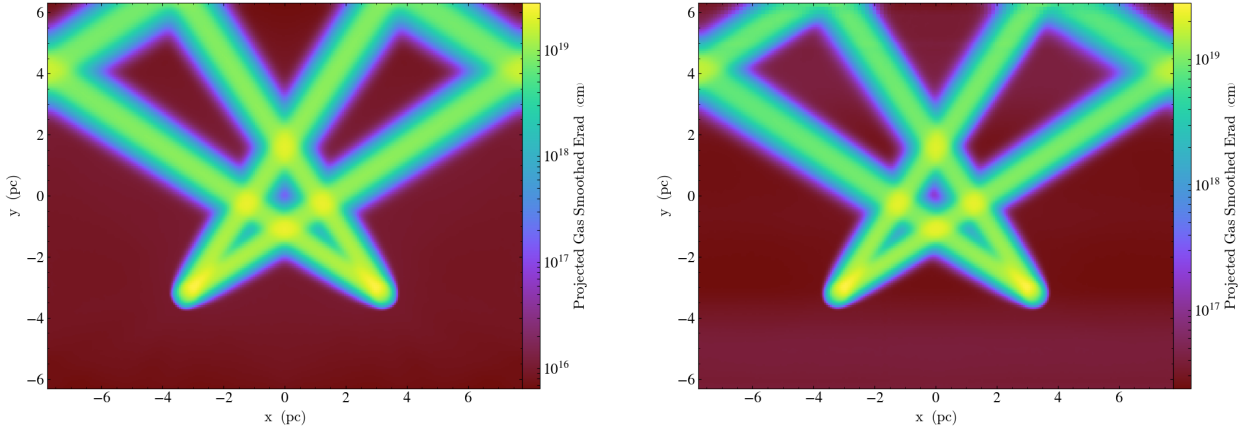


Figure 4. Projected E_r for a stationary fluid and mesh (left) and the moving fluid and mesh (right). In the right plot, the fluid moves in the $+x$ direction at a velocity of $v = 3 \text{ km s}^{-1}$, which is 30% of the reduced speed of light \bar{c}

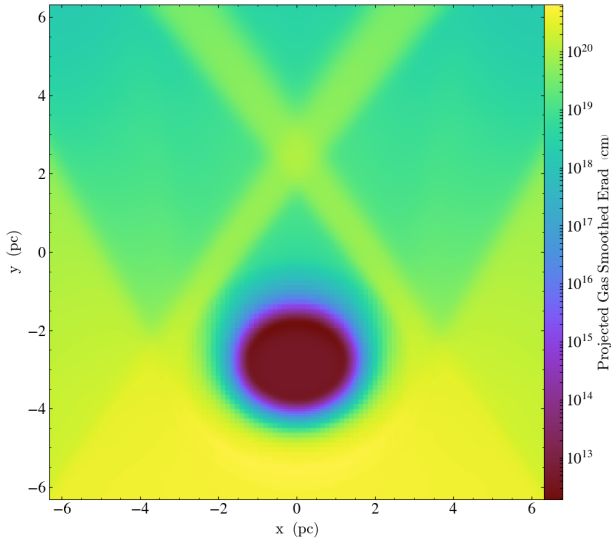


Figure 5. Projected E_r for a multiple shadow test. Radiation is emitted with a radiation temperature of $T_{\text{eff}} = 200 \text{ K}$ from the bottom boundary with angle $\theta = 0.98$ (56 degrees) and -0.98 from the y -axis. Two shadows will be produced and the shaded beams are also visible.

of a pure acoustic wave have a power law index of -1.74 with respect to linear resolution. This is nearly the same index found by [Yalinewich et al. \(2015\)](#), whose methods of gradient estimation we adopt in *MANGA* ([Chang et al. 2017](#)).

Although the integration and reconstruction scheme might be expected to yield second order convergence, the method is only formally first order since the implicit update of the radiation transfer source term is only first order in time. Hence, our first order convergence is consistent with this expectation. Nevertheless, we note that *JSD14* showed second-order convergence for the case of $\tau = 0.01$ and $\bar{c} = c$, which can be attributed to the limited impact of the radiation source term on the sound wave in this regime. Our convergence remains only first order for $\tau = 0.01$ with either

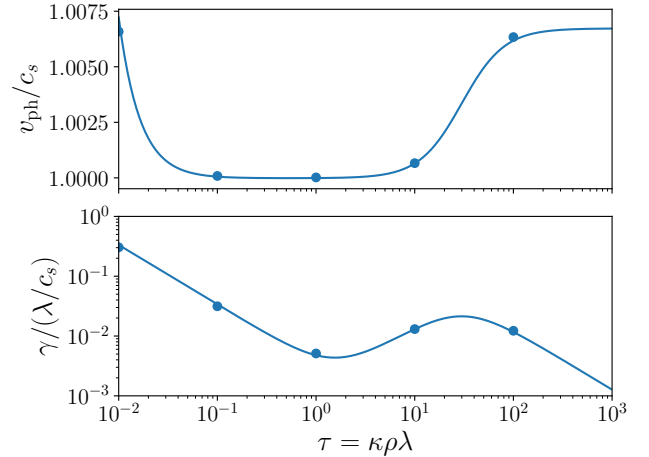


Figure 6. Phase velocity, $v_{\text{ph}} = \omega_r/k$, in units of the isothermal sound speed, c_s (top), and damping coefficient, γ (bottom), in units of λ/c_s for $P_{\text{rad}} = P_g$, $c/c_s = 1.45 \times 10^3$ and $c_r/c = 10^{-2}$ as a function of optical depth across a wavelength, τ_w . Solid dots are fits from the simulations.

$\bar{c} = 10^2 c$ or c , motivating further study to see if we can improve convergence in this weakly coupled regime.

Finally, we explore the effect of mesh regularity on the convergence of our result as previously discussed by [Pakmor et al. \(2016a\)](#). In Figure 8, we plot the L1 norm for the radiative linear wave with $\tau = 1$ and the pure acoustic wave for a nearly cartesian mesh (deviations in the mesh generating points of 10^{-6} of the separation, dx) and two cartesian meshes with deviation of 1% and 10% of the separation. For the acoustic wave, we can see that increasing non-regularity of the mesh degrades the second order convergence of the hydrodynamics solver, but the linear wave suffer no such degradation. Instead, its first-order convergence appears to be dominated by the radiation solver.

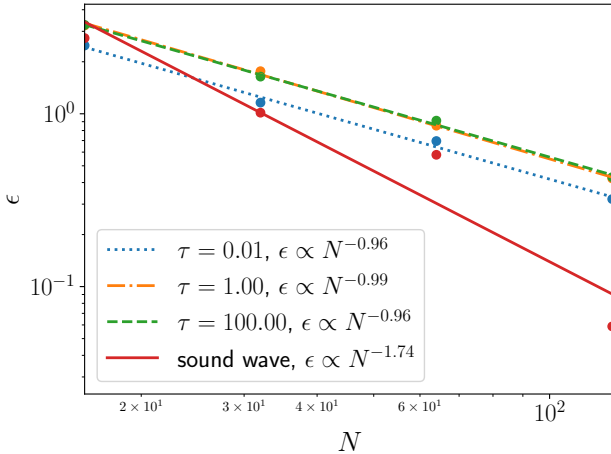


Figure 7. Error (as L1 norm) as a function of x-resolution, N , for $\tau = 0.01, 1, 100$, spanning the range from optically thin to thick. We also plot the error for a pure acoustic wave, which has an index of -1.74 , which is close to the expected second order convergence index of -2 . The convergence of the radiation cases are consistent with first order convergence.

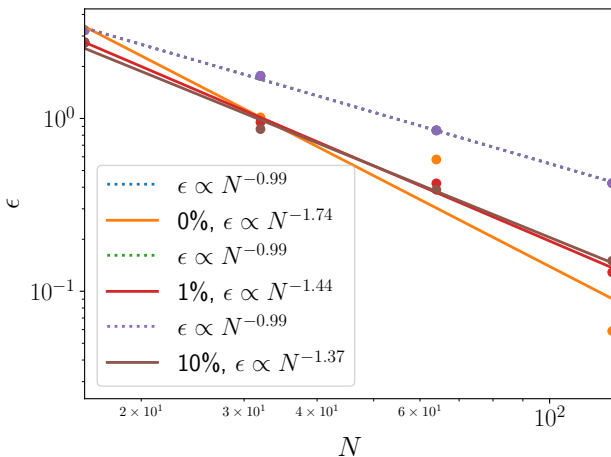


Figure 8. Error (as L1 norm) as a function of x-resolution for $\tau = 1$ and the pure acoustic wave for a nearly cartesian grid 0% deviation and two cartesian grids with a poisson deviation in the mesh generating points of 1% and 10% of the separation, dx . The radiative linear wave is dominated by the first-order convergence of the radiation solver, while the second order convergence of the sound wave is degrade by an increasingly non-regular mesh.

4 DISCUSSION AND CONCLUSIONS

We have adapted JSD14’s algorithm for radiation hydrodynamics based on solving the time-dependent RT equation to an unstructured MM and implemented it in the MM code, **MANGA**. We solve the specific intensities along different angles and integrate these intensities over angles to find the radiation energy and momentum source terms that coupled to the hydrodynamic equations. We have tested our implementation on a set of simple problems. These test problems show that energy and momentum between radiation

and matter is conserved by the implicit solver even when the coupling time between radiation and matter is much shorter than the characteristic timestep. Additionally, the crossing beam and multiple shadow tests demonstrate that the method produces qualitatively correct results in the optically thin limit when multiple sources and obstructions give rise to a complex radiation field. In particular, these latter two tests demonstrate the importance of the angular distribution of radiation in producing the qualitatively correct dynamics. As stated in JSD14, the principle advantage of this method is that the angular distribution of photons is calculated self-consistently. Because we do not use an ad-hoc closure relation as required in FLD and M1 methods, this method is generally superior in the optically thin case with complex radiation fields. Finally, we demonstrate the fidelity of our radiation hydrodynamics solver in reproducing an analytic results in the linear wave test and converges appropriately with higher resolution.

As mentioned by JSD14, the method of solving the time-dependent RT equations is more straightforward to implement than the method of short characteristics as it does not require a global solve. In addition JSD14 mentions that this method treats radiation and hydrodynamic variables on a similar footing. Thus, it is straightforward to extend it to curvilinear coordinate systems with nonuniform grids. Here, we recognized their insight by extending it to moving unstructured grids.

Our primary planned applications for this radiation module are dynamical stellar problems such as stellar mergers (Prust & Chang 2019) and tidal disruption events. Cases where radiation pressure blows material away may require the development of a grid regularization scheme. Radiation momentum driving tends to push material away from sources, which typically are a small fraction of the volume of a simulation box. As a result, moving meshes can quickly get distorted without some sort of mesh regularization that either keeps the volume or mass of each cell fairly regular or an algorithm to generate more mesh points to maintain mesh regularity (S10). By contrast gravity tends to pull material from the entire simulation volume into small regions, so the need for such algorithms, while desirable, is not required. For this reason, we have refrained from simulating radiation feedback problems (Krumholz & Thompson 2012; Davis et al. 2014; Rosdahl & Teyssier 2015), which Kannan et al. (2019) has recently demonstrated using AREPO-RT. We plan to implement a mesh regularization scheme for **MANGA** to address this need.

There are a number of improvements that would greatly improve the utility of the radiation solver. These include the inclusion of magnetic fields, alternative RT schemes, additional mesh generation/regularization improvements, and performance improvements. Here we note that the recent implementation of RT in Arepo-RT (Kannan et al. 2019), contains an ionization solver. We have no plans to implement ionization in our current scheme as the relevant science questions that we are interested in does not require it.

Implementation of alternative RT schemes would permit comparison between this full angular schemes and moment schemes such as FLD or M1. Here we have mentioned that limitation of M1 in producing the qualitatively correct solutions to various test problems such as the crossing beam test and double shadow test. At the same time, the full an-

gular implementation we use here suffers from angular discretization which for single sources may be at a disadvantage compared to M1. A detailed comparison between different RT schemes for specific problems is a problem worthy of further study.

Performance improvements for these various schemes are planned for the near future. Even in the reduced speed of light approximation, the reduced speed of light is usually at least a factor of a few faster than the fastest velocity, which limits the timestep. However, the radiative transfer solution can be greatly simplified compared to the hydrodynamic step in that the same Voronoi structure can be assumed to be constant across the step. As a result, sub-cycling the radiative transfer step may result in substantial computational savings as [Kannan et al. \(2019\)](#) have recently implemented in AREPO-RT.

The source code, test problems, and documentation for MANGA will be available with all the physics (MHD, radiation) in an anticipated future public release of ChaNGa. We hope that this code will find wide application in astrophysical problems. We encourage interested parties to contact us if they are interested in using MANGA before the public release.

ACKNOWLEDGEMENTS

We thank Norman Murray and Paul Duffell for useful discussions. We thank Jim Stone for useful discussions and for permission to use various code segments of Athena and Athena++ in MANGA. We thank the anonymous reviewer for a constructive report. PC is supported by the NASA ATP program through NASA grant NNH17ZDA001N-ATP, NSF CAREER grant AST-1255469, and the Simons Foundation. SWD acknowledge support from NSF grant AST-1616171 and an Alfred P. Sloan Research Fellowship. YFJ was supported in part by the National Science Foundation under Grant No. NSF PHY-1748958. We also used the Extreme Science and Engineering Discovery Environment (XSEDE), which is supported by National Science Foundation (NSF) grant No. ACI-1053575. We also acknowledge the Texas Advanced Computing Center (TACC) at The University of Texas at Austin for providing HPC resources that have contributed to the research results reported within this paper. URL: <http://www.tacc.utexas.edu>. We also use the yt software platform for the analysis of the data and generation of plots in this work ([Turk et al. 2011](#)). The Flatiron Institute is supported by the Simons Foundation.

REFERENCES

Chang P., Wadsley J., Quinn T. R., 2017, *MNRAS*, **471**, 3577
 Commerçon B., Teyssier R., Audit E., Hennebelle P., Chabrier G., 2011, *A&A*, **529**, A35
 Davis S. W., Stone J. M., Jiang Y.-F., 2012, *The Astrophysical Journal Supplement Series*, **199**, 9
 Davis S. W., Jiang Y.-F., Stone J. M., Murray N., 2014, *ApJ*, **796**, 107
 Duffell P. C., 2016, *ApJS*, **226**, 2
 Duffell P. C., MacFadyen A. I., 2011, *ApJS*, **197**, 15
 Gaburov E., Johansen A., Levin Y., 2012, *ApJ*, **758**, 103
 González M., Audit E., Huynh P., 2007, *A&A*, **464**, 429
 Hayes J. C., Norman M. L., 2003, *The Astrophysical Journal Supplement Series*, **147**, 197

Hopkins P. F., 2015, *MNRAS*, **450**, 53
 Jetley P., Gioachin F., Mendes C., Kale L. V., Quinn T. R., 2008, Proceedings of IEEE International Parallel and Distributed Processing Symposium
 Jetley P., Wesolowski F., Gioachin F., Kale L. V., Quinn T. R., 2010, Proceedings of the 2010 ACM/IEEE International Conference for High Performance Computin
 Jiang Y.-F., Stone J. M., Davis S. W., 2012, *The Astrophysical Journal Supplement Series*, **199**, 14
 Jiang Y.-F., Stone J. M., Davis S. W., 2014, *The Astrophysical Journal Supplement Series*, **213**, 7
 Jiang Y.-F., Stone J., Davis S. W., 2017, preprint, ([arXiv:1709.02845](https://arxiv.org/abs/1709.02845))
 Kale L. V., Krishnan S., 1996, in Wilson G. V., Lu P., eds., Parallel Programming using C++. MIT Press, pp 175–213
 Kannan R., Vogelsberger M., Marinacci F., McKinnon R., Pakmor R., Springel V., 2019, *MNRAS*, **485**, 117
 Krumholz M. R., Thompson T. A., 2012, *ApJ*, **760**, 155
 Krumholz M. R., Klein R. I., McKee C. F., Bolstad J., 2007, *ApJ*, **667**, 626
 Levermore C. D., Pomraning G. C., 1981, *ApJ*, **248**, 321
 McKinney J. C., Tchekhovskoy A., Sadowski A., Narayan R., 2014, *MNRAS*, **441**, 3177
 Menon H., Wesolowski L., Zheng G., Jetley P., Kale L., Quinn T., Governato F., 2015, *Computational Astrophysics and Cosmology*, **2**, 1
 Mihalas D., Klein R. I., 1982, *Journal of Computational Physics*, **46**, 97
 Miyoshi T., Kusano K., 2005, *Journal of Computational Physics*, **208**, 315
 Mocz P., Vogelsberger M., Hernquist L., 2014, *MNRAS*, **442**, 43
 Mocz P., Vogelsberger M., Pakmor R., Genel S., Springel V., Hernquist L., 2015, *MNRAS*, **452**, 3853
 Mocz P., Pakmor R., Springel V., Vogelsberger M., Marinacci F., Hernquist L., 2016, *MNRAS*, **463**, 477
 O’Connor E., Ott C. D., 2010, *Classical and Quantum Gravity*, **27**, 114103
 Ohlmann S. T., Röpke F. K., Pakmor R., Springel V., 2016, *ApJ*, **816**, L9
 Pakmor R., Bauer A., Springel V., 2011, *MNRAS*, **418**, 1392
 Pakmor R., Springel V., Bauer A., Mocz P., Muñoz D. J., Ohlmann S. T., Schaal K., Zhu C., 2016a, *MNRAS*, **455**, 1134
 Pakmor R., Pfrommer C., Simpson C. M., Kannan R., Springel V., 2016b, *MNRAS*, **462**, 2603
 Paxton B., Bildsten L., Dotter A., Herwig F., Lesaffre P., Timmes F., 2011, *ApJS*, **192**, 3
 Paxton B., et al., 2013, *ApJS*, **208**, 4
 Paxton B., et al., 2015, *ApJS*, **220**, 15
 Pfrommer C., Pakmor R., Schaal K., Simpson C. M., Springel V., 2017, *MNRAS*, **465**, 4500
 Prust L. J., Chang P., 2019, *MNRAS*, **486**, 5809
 Rosdahl J., Teyssier R., 2015, *MNRAS*, **449**, 4380
 Rybicki G. B., Lightman A. P., 1986, Radiative Processes in Astrophysics
 Schneider A. S., Roberts L. F., Ott C. D., 2017, *Phys. Rev. C*, **96**, 065802
 Shen S., Wadsley J., Stinson G., 2010, *MNRAS*, **407**, 1581
 Skinner M. A., Ostriker E. C., 2013, *The Astrophysical Journal Supplement Series*, **206**, 21
 Springel V., 2005, *MNRAS*, **364**, 1105
 Springel V., 2010, *MNRAS*, **401**, 791
 Stinson G., Seth A., Katz N., Wadsley J., Governato F., Quinn T., 2006, *MNRAS*, **373**, 1074
 Timmes F. X., Swesty F. D., 2000, *ApJS*, **126**, 501
 Toro E., 2009, Riemann Solvers and Numerical Methods for Fluid Dynamics: A Practical Introduction. Springer Berlin Heidelberg
 Turk M. J., Smith B. D., Oishi J. S., Skory S., Skillman S. W.,

- Abel T., Norman M. L., 2011, [The Astrophysical Journal Supplement Series](#), **192**, 9
- Turner N. J., Stone J. M., 2001, [The Astrophysical Journal Supplement Series](#), **135**, 95
- Vandenbroucke B., De Rijcke S., 2016, [Astronomy and Computing](#), **16**, 109
- Vogelsberger M., et al., 2014, [MNRAS](#), **444**, 1518
- Wadsley J. W., Keller B. W., Quinn T. R., 2017, [MNRAS](#), **471**, 2357
- White C. J., Stone J. M., Gammie C. F., 2016, [ApJS](#), **225**, 22
- Yalinewich A., Steinberg E., Sari R., 2015, [ApJS](#), **216**, 35
- Zhang D., Davis S. W., Jiang Y.-F., Stone J. M., 2018, [ApJ](#), **854**, 110
- Zhu C., Pakmor R., van Kerkwijk M. H., Chang P., 2015, [ApJ](#), **806**, L1
- van der Holst B., et al., 2011, [The Astrophysical Journal Supplement Series](#), **194**, 23

This paper has been typeset from a $\text{\TeX}/\text{\LaTeX}$ file prepared by the author.